Numerical Heat Transfer, Part B, 51: 141–157, 2007

ISSN: 1040-7790 print/1521-0626 online
DOI: 10.1080/10407790600878585

Taylor & Francis
Taylor & Francis Group

PARTICLE TRANSPORT IN MICROCHANNELS

Y. F. Yap, J. C. Chai, T. N. Wong, N. T. Nguyen, and K. C. Toh
School of Mechanical & Aerospace Engineering, Nanyang Technological University, Singapore

H. Y. Zhang
Institute of Microelectronics, Singapore

Particle transport in microchannel is presented. This article focuses on situations in which the sizes of the particles are comparable to the sizes of the channels. These solid bodies are sufficiently large that momentum is exchanged between the bodies and the flowing fluid. As a result, the solid bodies affect the fluid flow significantly, and vice versa, resulting in a transient process in which the motions of the solid bodies and the flow field are strongly coupled. The flow field and the particulate flow must then be solved simultaneously. The solid bodies are modeled as a fluid constraint to move with rigid body motion. The solid–fluid interface is described using a distance function. For demonstration purposes, the finite-volume method is used to solve the resulting set of governing equations. The present approach is validated against (1) flow around stationary, (2) flow around forced rotating, (3) flow around freely rotating cylinders, and (4) sedimentation of a circular cylinder under gravity. Finally, the motion of particles carried by an incompressible fluid in a microchannel system is studied.

INTRODUCTION

Solid–fluid flows are found in many engineering processes. The solid–fluid motions can be classified into two categories, discrete particulate flows and interrelated continua. The first type of solid–fluid flows is encountered in fluidization of solid fuel for combustion and separation of solid particles in flue gas using cyclones. Although the number of solid bodies involved in these processes is large, the size of the solid bodies is relatively small. In these situations, the interfaces between the phases are not important and therefore are not treated. Discrete particulate flows have been investigated in [1–3] for macrochannels and [4] for microchannels.

In the interrelated continua type of solid–fluid flow, the size of the solid particle is comparable to the size of the microchannel. These solid bodies are sufficiently large that momentum is exchanged between the bodies and the flowing fluid. As a result, the solid bodies affect the fluid flow significantly, and vice versa, resulting in a transient process in which the motions of the solid bodies and the flow field are strongly coupled. The flow field and the particulate flow must then be solved

Received 18 April 2006; accepted 16 June 2006.
Address correspondence to John C. Chai, Nanyang Technological University, School of Mechanical and Aerospace Engineering, Nanyang Avenue, Singapore 639798. E-mail: mckchai@ntu.edu.sg

NOMENCLATURE

a	semimajor axis of an ellipse
b	semiminor axis of an ellipse
C_D	coefficient of lift
C_L	coefficient of drag
d	diameter of a circular cylinder
dA	elemental area
D	Dirac delta function
e	dimensionless eccentricity parameter
F	force
F_D	drag force
F_L	lift force
$\vec{F}$	surface force
$\vec{g}$	gravitational acceleration
$\vec{G}$	body force
H	height of the domain
$\overline{\overline{I}}_i$	inertia tensor
$\hat{k}$	unit vector in the z direction
L	length of the domain
m	mass of the solid body
$\hat{n}$	unit normal at the interface
N	number of solid body
p	pressure
Re	Reynolds number
t	time
$\vec{T}$	torque
u	velocity component in the x direction
u_l	characteristic velocity
$\vec{u}$	velocity vector
$\vec{U}$	velocity vector of the centroid of a solid body
v	velocity component in the y direction
$\vec{x}$	position vector
α	fluid property
β	dimensionless rotational parameter
Γ	solid–fluid interface
ΔV	volume sandwiched between constant ϕ_i^+ and ϕ_i^- surfaces
ε	offset for the Dirac delta function
θ	angle between the semimajor axis of an ellipse and abscissa x
μ	viscosity
ρ	density
$\overline{\overline{\sigma}}$	stress tensor
ψ	parameter for the solid–fluid interface
ϕ	signed distance function
φ	parameter for the solid–fluid interface
Ω	z-component angular velocity
$\vec{\Omega}$	angular velocity vector

Subscripts

c	centroid of a solid body
f	fluid
i	solid body number
in	inlet condition
out	outlet condition
p	solid

simultaneously. Compared to single-phase flow in microchannels [5, 6], solid–fluid flow in microchannels seems to receive little attention.

Methods for interrelated continua solid–fluid two-phase flows can be classified into two broad categories. These are moving-mesh methods and fixed-mesh methods. In the moving-mesh methods, the solid–fluid interface is sharply described by a boundary-conforming mesh [7–10]. The mesh boundary is made to coincide with the solid–fluid interface. Appropriate solid–fluid interface conditions can be applied directly at the exact location. This provides good accuracy for the implementation of solid–fluid interface conditions. The mesh must follow the motion of the interface in order to capture the interface properly for all times. As the solid moves, a new boundary-conforming mesh is generated to capture the solid–fluid interface. Information is then transferred to the new mesh, on which further computations are made.

In the fixed-mesh methods, as the name implies, a fixed grid is employed for the whole computational domain for all times. Remeshing is therefore not required. This is the main advantage of fixed-mesh methods. The solid bodies are considered to be fluid with rigid body motions. Fixed-mesh methods include the fictitious domain approach [11], the fictitious boundary method [12], and a modified Cartesian grid method [13].

This article presents an approach for simulation of the flows of multiple solid bodies carried by an incompressible fluid using a finite–volume method [14]. A fixed staggered grid is employed. A distance function is employed to identify the solid bodies. The surface force and the associated torque induced by the flowing fluid are evaluated through a volume integration utilizing the Dirac delta function.

The remainder of the article is divided into four sections. The mathematical formulation of the present approach is presented first. In this section, the identification of the fluid–solid interfaces is detailed. With the fluid–solid interfaces identified, the governing equations are written for both fluid and solid bodies. Then, the construction of the distance function and calculation of the resultant surface force and torque on the solid bodies are given. The solution procedure and the relevant boundary conditions are presented to complete the mathematical formulation. The numerical method used in this article is then discussed. This is followed by validation of the proposed method and presentations of the results for particles flowing in a microchannel system. Finally, some remarks are given to conclude the article.

MATHEMATICAL FORMULATION

Figure 1 shows a ''two-phase'' problem in which N rigid solid bodies interact with a fluid flowing between two parallel plates. Here, ''two-phase'' refers to solid and fluid. The solid bodies are sufficiently large that momentum is exchanged between the bodies and the flowing fluid. As a result, the solid bodies affects the fluid flow significantly, and vice versa, resulting in a transient process in which the motions of the solid bodies and the flow field are strongly coupled. The solid bodies undergo both translational and rotational motions under the influence of these forces.

Identification of the Solids

A *local* signed distance function ϕ_i is introduced to identify the fluid–solid interface for each solid body. It is defined as the shortest signed normal distance from the fluid–solid interface of that particular solid body. A *global* distance

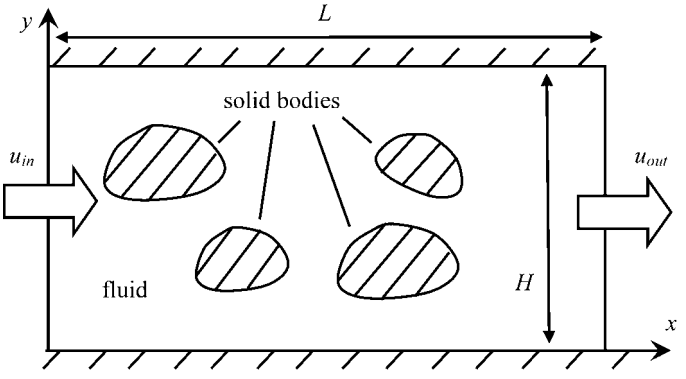

Figure 1. Flow of solid bodies in a fluid between two parallel plates.

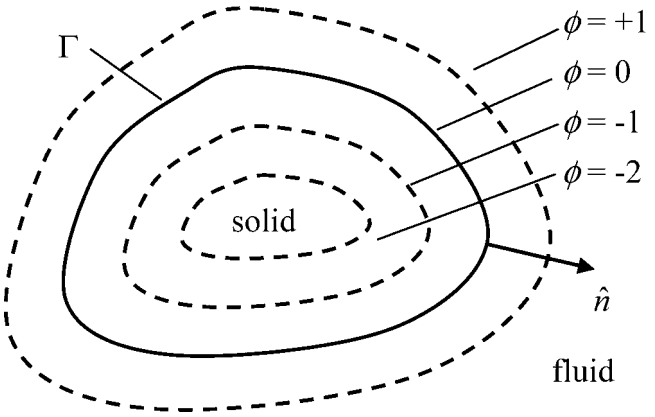

Figure 2. Surfaces of constant signed distance function ϕ.

function ϕ can then be constructed by combining all the local distance functions to represent the fluid–solid interface for all solid bodies. At the solid–fluid interfaces Γ, $\phi = 0$. Surfaces of constant ϕ around a typical solid body (dashed lines) are shown in Figure 2. The solid line represents the solid–fluid interface Γ. In order to differentiate the fluid region from the solid regions, ϕ of the fluid region can be assigned either a positive or a negative sign as long as ϕ of the solid region has an opposite sign. For ease of discussion and without loss of generality, ϕ of the fluid region is assigned a positive sign in this article. Therefore,

$$\phi(\vec{x}, t) = \begin{cases} < 0 & \text{if } \vec{x} \in \text{solid regions} \\ = 0 & \text{if } \vec{x} \in \Gamma \\ > 0 & \text{if } \vec{x} \in \text{fluid region} \end{cases} \tag{1}$$

where $\vec{x}$ and t are the position vector and time, respectively. With this choice of sign convention, the unit outward normal to the interface $\hat{n}$ can be expressed as

$$\hat{n} = \nabla\phi \tag{2}$$

Since ϕ is a distance function, it satisfies $|\nabla\phi| = 1$. The construction of both *local* and *global* signed distance functions will be detailed in a later section.

Continuity and Momentum Equations

In this article, an unsteady incompressible laminar flow is considered. The continuity and the momentum equations are

$$\nabla \cdot \vec{u} = 0 \tag{3}$$

$$\frac{\partial \vec{u}}{\partial t} + \vec{u} \cdot \nabla\vec{u} = -\frac{1}{\rho}\nabla p + \frac{\mu}{\rho}\nabla^2\vec{u} + \vec{g} \tag{4}$$

where $\vec{u}$, $\vec{g}$, p, ρ, and μ are the velocity vector, body force per unit mass, pressure, density, and viscosity, respectively. These equations apply to the whole domain. As such, ρ and μ represent the density and viscosity appropriate for the phase occupying the particular spatial location at a given instant of time. These properties are expressed as

$$\alpha(\phi) = \begin{cases} \alpha_p & \phi < 0 \\ \alpha_f & \phi > 0 \end{cases} \tag{5}$$

where α can be either density or viscosity. The subscripts p and f denote solid bodies and fluid, respectively. The solid bodies are modeled as a highly viscous fluid. With this, the "fluids" in the solid regions behave as rigid bodies and are therefore constrained to move with rigid body motions.

Solid Body Motion

The translational motion of the ith solid body is governed by

$$m_i \frac{d\vec{U}_i}{dt} = \vec{F}_i + \vec{G}_i \tag{6}$$

where m_i and $\vec{U}_i$ are the mass and the translational velocity vector (of the centroid) of the ith solid body. The resultant surface and the body forces are denoted as $\vec{F}_i$ and $\vec{G}_i$, respectively. The rotational motion of the ith solid body is governed by

$$\bar{\bar{I}}_i \frac{d\vec{\Omega}_i}{dt} + \vec{\Omega}_i \times \bar{\bar{I}}_i \vec{\Omega}_i = \vec{T}_i \tag{7}$$

where $\bar{\bar{I}}_i$ and $\vec{\Omega}_i$ represent the inertia tensor and the angular velocity vector of the ith body, respectively. The torque induced by the surface force is denoted as $\vec{T}_i$.

The location of the centroid and the orientation of the ith body in the course of its motion are calculated through

$$\vec{U}_i = \frac{d\vec{x}_{c,i}}{dt} \tag{8}$$

$$\Omega_i = \frac{d\theta_i}{dt} \tag{9}$$

with the initial conditions of

$$\vec{x}_{c,i}(t=0) = \vec{x}_{c,io} \tag{10a}$$

$$\theta_i(t=0) = \theta_{io} \tag{10b}$$

Calculation of Surface Force and Torque on a Solid Body

The resultant surface force $\vec{F}_i$ acting at the centroid of the ith solid body is given by

$$\vec{F}_i = \int_{\Gamma_i} \overline{\overline{\sigma}} \cdot \hat{n}\, dA \tag{11}$$

where Γ_i, dA, $\overline{\overline{\sigma}}$, and $\hat{n}$ are the interfacial area between the ith solid body and the fluid, the infinitesimal interfacial area, the stress tensor, and the unit outward normal of the interface, respectively. In this article, the surface integral is transformed into a volume integral around Γ_i. Equation (11) is rewritten as

$$\vec{F}_i = \int_{\Delta V} D(\phi_i - \varepsilon)\overline{\overline{\sigma}} \cdot \hat{n}\, dV \tag{12}$$

where $D(\phi_i - \varepsilon)$ and ΔV are a Dirac delta function and the volume sandwiched between the constant $\phi_i = 0$ and $\phi_i = 2\varepsilon$ surfaces. Note that ϕ_i is the *local* distance function for the ith solid body. As a result, the resultant surface force $\vec{F}_i$ [Eq. (11)] is reformulated into an equivalent body force [Eq. (12)]. It now acts within a volume defined by $0 \leq \phi_i \leq 2\varepsilon$, rather than concentrating at the interface Γ_i. The integration is performed over the fluid side of the interface because the force on the solid is exerted by the fluid flowing next to the solid. The Dirac delta function $D(\phi_i - \varepsilon)$ is defined such that

$$D(\phi_i - \varepsilon) = \begin{cases} (1 + \cos[\pi(\phi_i - \varepsilon)/\varepsilon])/(2\varepsilon) & 0 \leq \phi_i \leq 2\varepsilon \\ 0 & \text{otherwise} \end{cases} \tag{13}$$

where ε is a parameter proportional to the mesh size. It is taken to be the smallest length of the control volumes. The distribution of $D(\phi_i - \varepsilon)$ is shown in Figure 3.

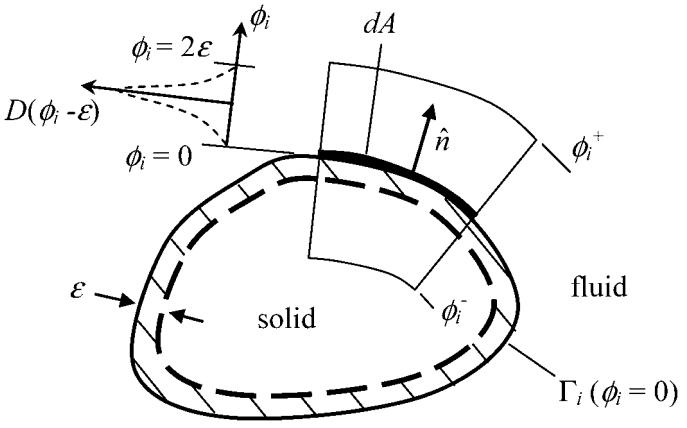

Figure 3. Distribution of $D(\phi_i - \varepsilon)$ across the solid–fluid interface Γ_i.

The Dirac delta function $D(\phi_i - \varepsilon)$ has the following property:

$$\int_{\phi_i^-}^{\phi_i^+} D(\phi_i - \varepsilon) d\phi_i = \begin{cases} 1 & \phi_i^- \le 0 \text{ and } \phi_i^+ \ge 2\varepsilon \\ 0 & \phi_i^- < \phi_i^+ \le 0 \text{ or } 2\varepsilon \le \phi_i^- < \phi_i^+ \end{cases} \tag{14}$$

Similarly, the torque $\vec{T}_i$ acting on the solid body is given by

$$\vec{T}_i = \int_{\Delta V} D(\phi_i - \varepsilon)(\vec{x} - \vec{x}_{c,i}) \times \bar{\bar{\sigma}} \cdot \hat{n}\, dV \tag{15}$$

Construction of the *Local* (for the *i*th Solid Body) Signed Distance Function ϕ_i

Suppose that there are N solid bodies in the domain at time t. Each solid body is represented by a *local* distance function ϕ_i, $i = 1, \ldots, N$. For the ith solid body, $\phi_i < 0$ inside the ith solid body and $\phi_i > 0$ outside the body.

Figure 4 shows an inclined elliptical body with its centroid located at $\vec{x}_{c,i}$. It has a major axis of $2a$ and a minor axis of $2b$. The elliptical body is inclined at an angle θ_i to the x axis. Surfaces of constant ϕ_i are shown in Figure 4 as dashed ellipses. Each of these constant ϕ_i ellipse is at equal distance from the interface Γ_i. To calculate ϕ_i, a new Cartesian coordinate $Ox'y'$ is introduced. This coordinate is related to the original coordinate Oxy via

$$\begin{pmatrix} x' \\ y' \end{pmatrix} = \begin{pmatrix} \cos\theta_i & \sin\theta_i \\ -\sin\theta_i & \cos\theta_i \end{pmatrix} \begin{pmatrix} x \\ y \end{pmatrix} \tag{16}$$

The constant ϕ_i ellipses are given by

$$\frac{(x' - x'_c)^2}{(a + \phi_i)^2} + \frac{(y' - y'_c)^2}{(b + \phi_i)^2} = 1 \tag{17}$$

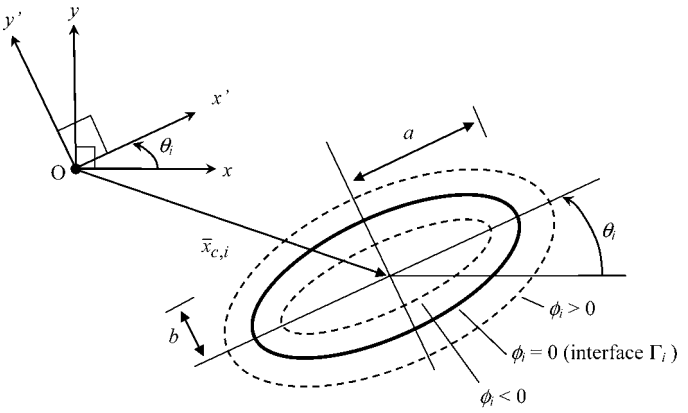

Figure 4. Description of ith elliptical body using two different coordinate systems.

where $\vec{x}'_{c,i} \equiv (x', y')$ is the centroid of the body with respect to the $Ox'y'$ coordinate system. Circular objects can be modeled by setting $a = b$.

Construction of the *Global* Signed Distance Function ϕ

The *global* distance function ϕ is constructed once all the *local* distance functions are obtained. The procedure for the construction of the global ϕ is described here.

1. Set the solid index i to 1.
2. Calculate $\vec{x}'_{c,i}$ using Eq. (16).
3. Select a control volume P and calculate $\vec{x}'_{P,i}$ corresponding to $\vec{x}_{P,i}$ using Eq. (16).
4. Solve Eq. (17) for ϕ_i (for the selected control volume P).
5. Repeat steps 3 and 4 for all control volumes.
6. If $i = 1$, set $\phi = \phi_i$.
7. Set $\phi = \text{MIN}[\phi, \phi_i]$.
8. Repeat steps 2–7 for all N solid bodies.

Boundary Conditions

At the inlet, the normal velocity is set to the inlet velocity u_{in} while the tangential velocity is set to zero. No-slip condition is applied at the bounding walls. At the outlet, the normal velocity is calculated to ensure mass conservation, while the axial gradient of the tangential velocity is set to zero.

The interface Γ_i of every solid body serves as the moving boundary for the fluid. The condition at the moving boundary Γ_i is imposed in the following manner. An inner layer of the ith solid body, defined as $-\varepsilon \leq \phi_i \leq 0$ (the shaded region in Figure 3), is set to be in rigid body motion. The velocities in this region are specified as

$$\vec{u} = \overrightarrow{U}_i + \Omega_i \hat{k} \times (\vec{x} - \vec{x}_{c,i}) \tag{18}$$

where the first and the second terms on the right represent the translational and the rotational motions, respectively. The velocity in the remaining region of the solid body defined by $\phi_i < -\varepsilon$ is forced to be zero. The setting of the velocity in these two regions of the solid body is achieved using the internal control-volume approach of Patankar [14]. This somewhat clumsy implementation of the particle motion using a two-region solid is presented so that future extension to model slip velocities (of unequal magnitude) can be implemented easily.

Solution Procedure

The whole solution procedure can be summarized as follows.

1. Define $\vec{x}_{c,io}$ and θ_{io} for $i = 1, \ldots, N$.
2. Construct the local ϕ_i and global ϕ.
3. Calculate ρ and μ using Eq. (5).

4. Solve Eqs. (3) and (4) for $\vec{u}$ and p.
5. Calculate $\overrightarrow{F_i}$ and $\overrightarrow{T_i}$ for $i = 1, \ldots, N$ using Eqs. (12) and (15).
6. Calculate $\vec{x}_{c,i}$ and θ_i for $i = 1, \ldots, N$ using Eqs. (8) and (9).

Repeat steps 2–6 for all time steps.

NUMERICAL METHOD

In this article, the finite-volume method (FVM) of Patankar [14] is used to solve the governing equations. Since a detailed discussion of the FVM is available in [14], only a very brief description of the major features of the FVM used is given here.

In the FVM, the domain is divided into a number of control volumes such that there is one control volume surrounding each grid point. The grid points are located in the centers of control volumes. The governing equation is integrated over each control volume to derive an algebraic equation containing the grid-point values of the dependent variable. The discretization equation then expresses the conservation principle for a finite control volume just as the partial differential equation expresses it for an infinitesimal control volume. The resulting solution implies that the integral conservation of quantities such as mass, momentum, and energy is satisfied for any control volume and, of course, for the whole domain. The power-law scheme is used to model the combined convection-diffusion effect in the transport equations. The SIMPLER algorithm is used to resolve the pressure–velocity coupling. The resulting algebraic equations are solved using a line-by-line tri-diagonal matrix algorithm.

RESULTS AND DISCUSSION

The proposed approach is validated using (1) flows around stationary, (2) flow around forced rotating, and (3) flow around freely rotating circular cylinders. Further validation is made for the case of a settling circular cylinder under gravity. With these validations, the flow of particles in a microchannel system is then considered. The Reynolds number, Re, the lift coefficient, C_L, and the drag coefficient, C_D, are defined as

$$\mathrm{Re}_{l_c} = \frac{\rho u_c l_c}{\mu} \tag{19a}$$

$$C_L = \frac{2F_L}{\rho u_c^2 l_c} \tag{19b}$$

$$C_D = \frac{2F_D}{\rho u_c^2 l_c} \tag{19c}$$

where u_c and l_c are the characteristic velocity and the characteristic length, respectively.

Flow around Circular Cylinders

Figure 5*a* shows a circular cylinder of diameter d, centered at (x_c, y_c) in a two-dimensional channel. The length and height of the channel are L and H, respectively. The average inlet velocity of the fluid is u_m. The moving fluid exerts a drag force F_D and lift force F_L on the cylinder.

The drag forces on flow around a stationary and a nonrotating cylinder in an infinite domain subjected to a uniform inlet velocity are predicted. Both the length L and height H are set to 200 times the diameter d to simulate an infinite domain. Nonuniform mesh with finer mesh clustered around the cylinder is used to capture the flow field near the cylinder. The predictions obtained using the proposed

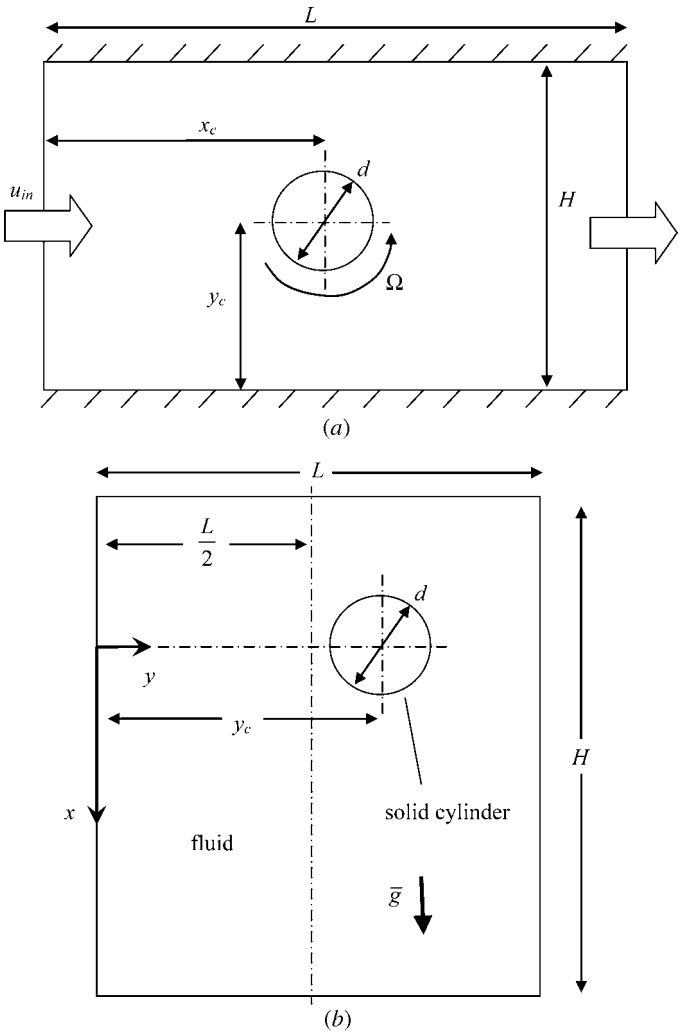

Figure 5. (*a*) Flow around a circular cylinder in a two-dimensional channel. (*b*) Sedimentation of a circular cylinder between parallel plates.

Table 1. C_D for flow around a stationary cylinder

Re	Present	[15]	[16]	[17]	[18]	[19]	[20]	[21]	[22]
1	11.596	—	—	9.94	—	—	—	11.00	12.55
10	2.855	2.81	2.78	2.67	—	—	—	3.15	—
20	2.065	2.01	2.01	2.08	2.05	2.03	2.22	2.36	—
40	1.547	1.54	1.51	1.73	1.52	1.52	1.48	1.85	—

approach are tabulated in Table 1. The present predictions compare well with available results [15–22] up to Re = 40.

The same problem is repeated, but now with the cylinder rotating at a constant angular velocity Ω. In addition to the Reynolds number Re, a dimensionless angular velocity $\beta = \Omega d/(2u_m)$ is defined to characterize the flow. Table 2 shows comparisons between the current predictions and available data. As expected, the angular rotation generates a nonzero lift force leading to a nonzero C_L. The present solutions compare well with those obtained from the full Navier-Stokes (NS) equations [23] and using series expansion (SE) [24] solutions.

In the next problem, a stationary (nontranslating) cylinder is placed off-center with an eccentricity $e = (2y_c - H)/(H - d)$ between two parallel plates. The length L, height H, and x_c are $27.5d$, $4d$, and $7.5d$, respectively. Fully developed flow enters the channel at $x = 0$. The characteristic velocity and characteristic length are the maximum inlet velocity (at $y = H/2$) and the diameter of the cylinder, respectively. As the cylinder is placed eccentrically, lift force and torque are generated. Two situations, (1) fixed (nonrotating) cylinder and (2) freely rotating cylinder, are investigated. Table 3 shows comparisons between the present computations and available results of [25]. Again, the lift and drag coefficients match available solutions well for both cases. The dimensionless angular velocity β for both cases is also tabulated for completeness.

Thus far, the procedure is capable of a modeling stationary (nontranslating) cylinder which rotates about a fixed stationary axis. The proposed procedure is now used to model translation and rotation.

Table 2. C_L and C_D for flow around a forced rotating cylinder

		C_L			C_D		
Re	β	NS [23]	SE [24]	Present	NS [23]	SE [24]	Present
5	0	0	0	6.5×10^{-13}	3.947	3.947	4.1239
5	0.5	1.389	1.384	1.3979	3.916	3.929	4.0917
5	1.0	2.838	2.768	2.8142	3.849	3.875	3.9958
20	0	0	0	2.1×10^{-14}	1.995	1.995	2.0512
20	0.5	1.283	1.271	1.2653	1.973	1.959	2.0164
20	1.0	2.617	2.541	2.5618	1.925	1.886	1.9138
60	0	0	0	3.3×10^{-12}	1.279	1.279	1.3094
60	0.5	1.109	1.085	1.0591	1.251	1.264	1.2812
60	1.0	2.249	2.170	2.1983	1.207	1.219	1.1876

Table 3. C_L and C_D for flow around a cylinder (Re = 100, $e = 5/6$)

		C_L		C_D	
Cylinder	β	[25]	Present	[25]	Present
Fixed	0	−0.3798	−0.37383	0.9440	0.93407
Freely rotating	0.07497	−0.4644	−0.46332	0.8949	0.88416

Sedimentation of a Circular Cylinder

Figure 5*b* shows the schematic of the problem. A circular cylinder of diameter d is placed at $(0, y_c)$ between two parallel plates spaced $4d$ apart. The cylinder, which is heavier than the fluid, is initially at rest. When it is released, it travels downward due to gravity. It will eventually reach its terminal velocity u_t. The diameter of the cylinder and its terminal velocity are the characteristic length and the characteristic velocity, respectively. The trajectories of the cylinder (Re = 0.522) released at different lateral locations off the centerline are shown in Figure 6. The results from the present

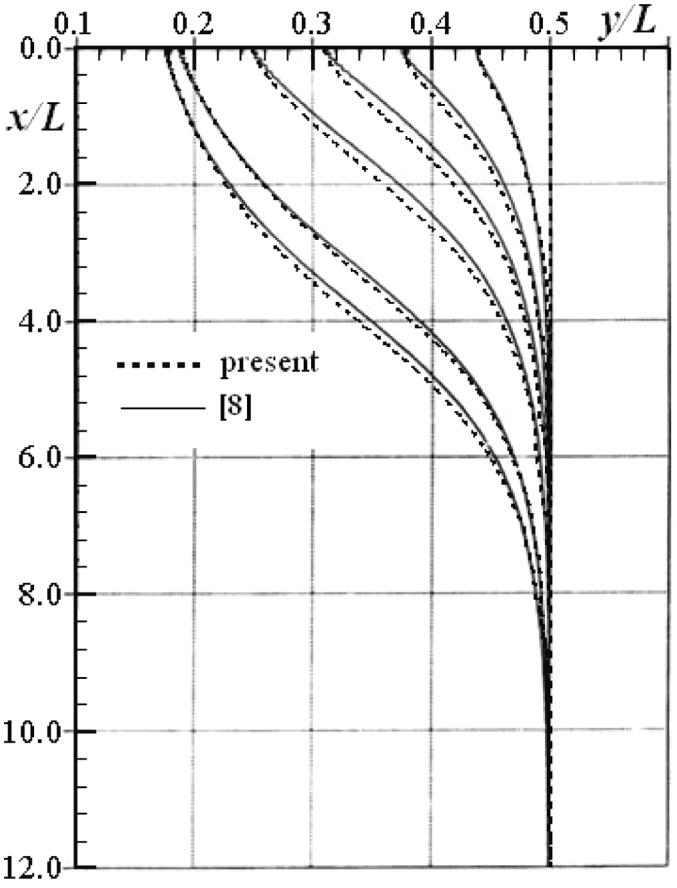

Figure 6. Settling trajectories of a circular cylinder under gravity for Re = 0.522.

computation compare well with those reported in the literature [8]. The slight differences between the two solutions are due to the significantly enlarged horizontal axis. As seen, the cylinder drifts toward the centerline for the Re studied.

Flow of Particles in a Microchannel System

Figure 7 shows a microchannel system with two inlets (A and B) and two outlets (C and D). A primary stream of carrier fluid flows into the system via inlet A. Another secondary stream of carrier fluid carrying solid particles is injected into the primary stream through inlet B. The fluid merges, flows through a constriction, and exits through one of the two outlets (C and D). The motion of the particle is determined by the resultant force due to hydrodynamics and inertia effects. The inertia of the particle acts to maintain its original course and the hydrodynamic force steers the particle to travel along the streaklines. Therefore, as the inertia of the particle increases, the motion of the particle deviates from the streakline of the carrier fluid. Depending on the flow condition, particle size, etc., a particle can exit through either of the exits.

The motion of a single circular solid particle is considered first. The solid particle, initially located at (x_c, y_c), is at rest. Water, with a density and a viscosity of $1{,}000\,\mathrm{kg/m^3}$ and $0.001\,\mathrm{Ns/m^2}$, respectively, is used as the carrier fluid. The inlet velocities u_A and u_B are set to $1{,}000\,\mu\mathrm{m/s}$ and $4{,}000\,\mu\mathrm{m/s}$, respectively.

The motion of a 30-μm-diameter aluminum particle initially located at (140, 104) is investigated. Figure 8 shows the trajectories of the particle obtained using a time-step size of $\Delta t = 2.50 \times 10^{-5}$ s with 151×118 control volumes (CVs) and $\Delta t = 1.25 \times 10^{-5}$ s with 302×236 CVs. The locations of the particle for every 1.25×10^{-2} s are shown for comparison purposes. It can be seen that a time-step size

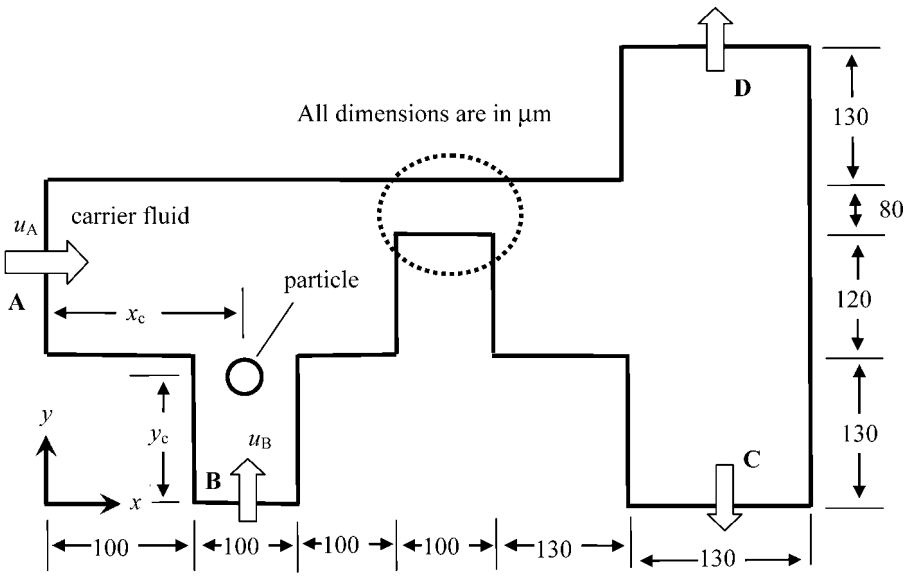

Figure 7. Schematic for flow of a solid particle in a microchannel system.

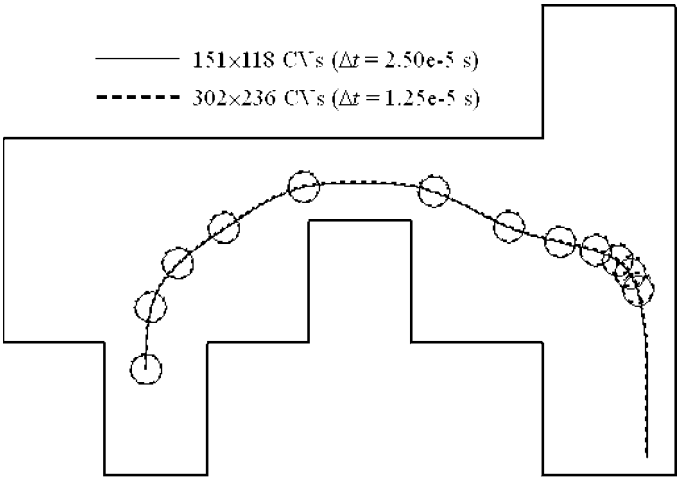

Figure 8. Grid-independence study.

of $\Delta t = 2.50 \times 10^{-5}$ s with 151×118 CVs produces a grid-independent solution. As a result, all subsequent computations are performed using this time step and mesh size.

As expected, the particle gains speed (particles spaced farther apart for a fixed Δt of 1.25×10^{-2} s), reaching a maximum velocity inside the constriction. As the flow bifurcates and leaves through the two exits, the particle slows down and travels toward exit C.

Figure 9 shows the effect of particle size on its trajectory. Initially, aluminum particles of two different diameters, 30 μm and 50 μm, are placed at (137, 104). The

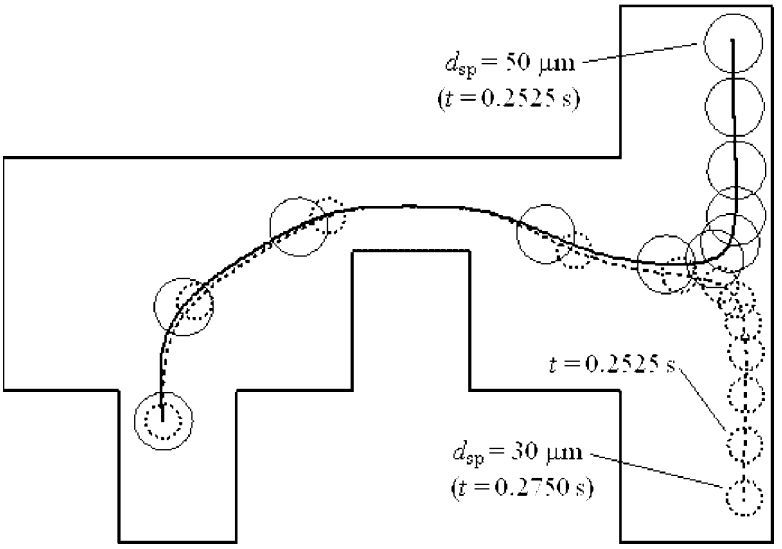

Figure 9. Effect of particle size on its trajectory.

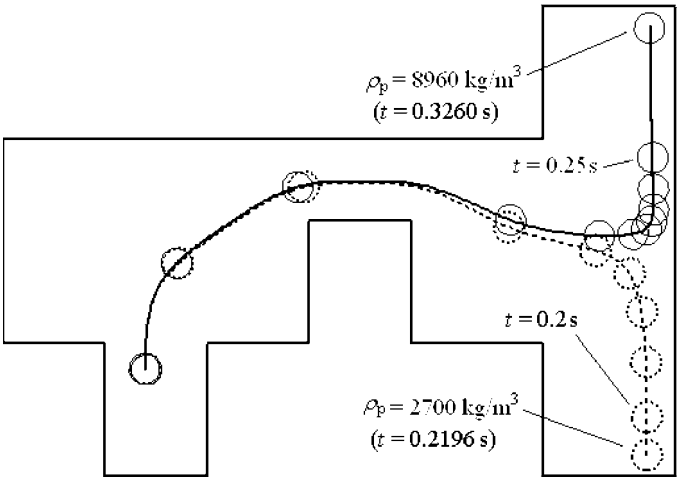

Figure 10. Effect of particle density on its trajectory.

particles travel along two different trajectories. The 30-μm and 50-μm particles are carried by the carrier fluid to outlet C and outlet D, respectively. The locations of the particle for every 2.5×10^{-2} s are shown for comparison purposes.

Figure 10 shows the effect of particle density on its trajectory. The particles are initially placed at (140, 104). The densities of the particles are set to 2,700 $\mathrm{kg/m^3}$ (aluminum) and 8,960 $\mathrm{kg/m^3}$ (copper). The hydrodynamic force on these particles of different densities but of identical size does not vary much. However, a denser

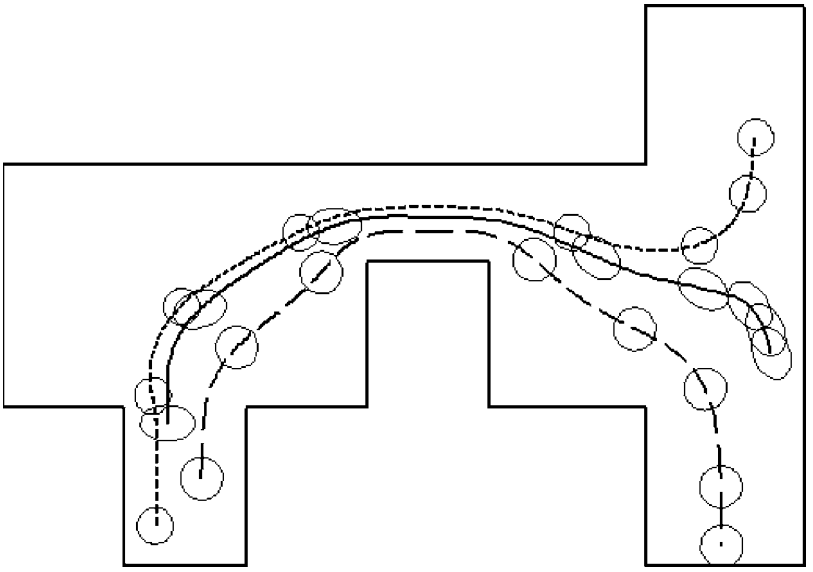

Figure 11. Trajectories of three particles flowing in a microchannel system.

particle implies a larger mass. The acceleration caused by the same hydrodynamic force on a denser particle is therefore smaller. As a result, denser particles move with a lower velocity and take longer to reach the outlet. This effect is more obvious after the particles enter the T junction.

Figure 11 shows the trajectories of three copper particles flowing in the microchannel system. There are two circular particles and an elliptical copper particle. A 30-μm-diameter circular particle is initially located at (125, 32.5). A larger (35-μm-diameter) circular particle is initially located at (163, 71.5). The major and minor axes of the elliptical particle are 45 and 30 μm, respectively. This elliptical particle is initially located at (135, 117). All three particles are initially at rest. The larger circular particle and the elliptical particles are driven to outlet C, while the smaller circular particle is carried to outlet D. The positions of these particle at eight time steps, $t = 0$ s, 0.025 s, 0.050 s, 0.075 s, 0.100 s, 0.125 s, 0.150 s, and 0.1675 s, are shown. The velocity of these particles is highest when they are flowing through the constriction.

CONCLUDING REMARKS

In this article, particle transport in microchannels has been modeled using a fixed-grid method. This article focuses on situations in which the particles are of comparable size to the microchannels. In such situations, the particle affects the fluid flow field and vice versa. The method was validated using (1) flow around stationary, (2) flow around forced rotating, (3) flow around freely rotating circular cylinders, and (4) a circular cylinder settling under gravity. It was then used to model particle flow in a microchannel system. The method presented here can be used to model particle transport in microchannels and particle separation process.

REFERENCES

1. F. Mashayek and D. B. Taulbee, Turbulent Gas–Liquid Flows I: Direct Simulations and Reynolds Stress Closures, *Numer. Heat Transfer B*, vol. 41, pp. 1–29, 2002.
2. H. Q. Zhang, C. K. Chan, and K. S. Lau, Numerical Simulation of Sudden-Expansion Particle-Laden Flows Using an Improved Stochastic Separated Flow Model, *Numer. Heat Transfer A*, vol. 40, pp. 89–102, 2001.
3. Y. Y. Niu and C. S. Tsai, Simulation of Erosion by the Dilute Particulate Flow Impact, *Numer. Heat Transfer A*, vol. 37, pp. 167–187, 2000.
4. Y. L. Hao and Y. X. Tao, A Numerical Model for Phase-Change Suspension Flow in Microchannels, *Numer. Heat Transfer A*, vol. 46, pp. 55–77, 2004.
5. S. L. Broderick, B. W. Webb, and D. Maynes, Thermally Developing Electroosmotic Convection in Microchannels with Finite Debye-Layer Thickness, *Numer. Heat Transfer A*, vol. 48, pp. 941–964, 2005.
6. P. Dutta, A. Beskok, and T. C. Warburton, Numerical Simulation of Mixed Electroosmotic/Pressure Driven Microflows, *Numer. Heat Transfer A*, vol. 41, pp. 131–148, 2002.
7. H. S. Udaykumar, H. Kan, W. Shyy, and R. Tran-Sob-Tay, Multiphase Dynamics in Arbitrary Geometries on Fixed Cartesian Grids, *J. Comput. Phys.*, vol. 137, pp. 366–405, 1997.
8. J. Feng, H. H. Hu, and D. D. Joseph, Direct Simulation of Initial Value Problems for the Motion of Solid Bodies in a Newtonian Fluid Part 1: Sedimentation, *J. Fluid Mech.*, vol. 261, pp. 95–134, 1994.

9. J. Feng, H. H. Hu, and D. D. Joseph, Direct Simulation of Initial Value Problems for the Motion of Solid Bodies in a Newtonian Fluid Part 2: Couette and Poiseuille Flows, *J. Fluid Mech.*, vol. 277, pp. 271–301, 1994.
10. P. Phutthavong and I. Hassan, Transient Performance of Flow over a Rotating Object Placed Eccentrically inside a Microchannel—Numerical Study, *Microfluid Nanofluid*, vol. 1, pp. 71–85, 2004.
11. R. Glowinski, T. W. Pan, T. I. Hesla, and D. D. Joseph, A Distributed Lagrange Multiplier/Fictitious Domain Method for Particulate Flows, *Int. J. Multiphase Flows*, vol. 25, pp. 755–794, 1999.
12. S. Turek, D. C. Wand, and L. S. Rivkind, The Fictitious Boundary Method for the Implicit Treatment of Dirichlet Boundary Conditions with Applications to Incompressible Flow Simulation, Challenges in Scientific Computing, *Lecture Notes in Computational Science and Engineering*, vol. 35, pp. 37–68, 2003.
13. C. Duchanoy and T. R. G. Jongen, Efficient Simulation of Liquid-Solid Flows with High Solids Fraction in Complex Geometries, *Comput. Fluids*, vol. 32, pp. 1453–1471, 2003.
14. S. V. Patankar, *Numerical Heat Transfer and Fluid Flow*, Hemisphere, New York, 1980.
15. A. L. F. Lima E Silva, A. Silveira-Neto, and J. J. R. Damasceno, Numerical Simulation of Two-Dimensional Flows over a Circular Cylinder Using the Immersed Boundary Method, *J. Comput. Phys.*, vol. 189, pp. 351–370, 2003.
16. J. Park, K. Kwon, and H. Choi, Numerical Solutions of Flow Past a Circular Cylinder at Reynolds Number up to 160, *Korean Soc. Mech. Eng. Int. J.*, vol. 12, p. 1200, 1998.
17. D. Sucker and H. Brauer, Fluiddynamik bei der angestromten Zilindern, *Wärme Stöffubertrag.*, vol. 8, p. 149, 1975.
18. S. C. R. Dennis and G. Chang, Numerical Solutions for Steady Flow past a Circular Cylinder at Reynolds Numbers up to 100, *J. Fluid Mech.*, vol. 42, p. 471, 1970.
19. T. Ye, R. Mittal, H. S. Udaykumar, and W. Shyy, An Accurate Cartesian Grid Method for Viscous Incompressible Flows with Complex Boundaries, *J. Comput. Phys.*, vol. 156, pp. 209–240, 1999.
20. D. J. Triton, Experiments on the Flow Past a Circular Cylinder at Low Reynolds Number, *J. Fluid Mech.*, vol. 6, p. 547, 1959.
21. F. M. White, *Viscous Fluid Flow*, McGraw-Hill, New York, 1991.
22. S. Tomotika and T. Aoi, An Expansion Formula for the Drag on a Circular Cylinder Moving through a Viscous Fluid at Small Reynolds Number, *Quart. J. Mech. Appl. Math.*, vol. 4, pp. 401–406, 1951.
23. D. B. Ingham and T. Tang, A Numerical Investigation into the Steady Flow past a Rotating Circular Cylinder at Low and Intermediate Reynolds Numbers, *J. Comput. Phys.*, vol. 87, pp. 91–107, 1990.
24. T. Tang and D. B. Ingham, On Steady Flow Past a Rotating Circular Cylinder at Reynolds Numbers 60 and 100, *Comput. Fluids*, vol. 19, pp. 217–230, 1991.
25. H. Juárez, R. Scott, R. Metcalfe, and B. Bagheri, Direct Simulation of Freely Rotating Cylinders in Viscous Flows by High-Order Finite Element Methods, *Comput. Fluids*, vol. 29, pp. 547–582, 2000.